Chapter 3
Spin-Polarized Plasmonics: Fresh View on Magnetic Nanoparticles

Vladimir P. Drachev, Maria Pogodaeva, Sergey V. Levchenko, and Ali E. Aliev

Abstract Here we discuss effect of spin-polarization on plasmon excitation in deep ultra-violet spectral range for Co nanoparticles with a single-domain magnetic structure. Structural, magnetic, and optical characterizations of Co nanoparticles shine a light on a mechanism of the magneto-plasmonic response.

3.1 Introduction

It is a common belief that the quality of the plasmon resonance of magnetic nanoparticles such as Co is quite low, which follows, in particular, from the experimental data for permittivity of bulk cobalt by Johnson and Christy (J&C) [1]. Our recent paper shows that for single-domain magnetic nanoparticles the usual approach, based on bulk permittivity, does not work, while used to work perfectly for nonmagnetic nanoparticles [2]. Indeed, our experiments prove that Co nanoparticles with a single-domain magnetic structure support a sharp plasmon resonance at about 280 nm with the resonance quality comparable to gold nanoparticles. This type of plasmons is quite different from known plasmons in noble metals. Note that the plasmon resonance of Co is in the deep ultraviolet spectral range, which is the range for bio-molecule resonances [3], as it is shown in Fig. 3.1, and, therefore, attractive for bio-medical applications in addition to its magnetic nature.

Deep ultraviolet (DUV) Raman spectroscopy selectively visualizes nucleotide bases, monomeric units of deoxyribonucleic acids (DNA) and aromatic amino acids, monomeric units of proteins, in cells due to the resonant effect (spectra are presented

V. P. Drachev (✉) · M. Pogodaeva · S. V. Levchenko
Skolkovo Institute of Science and Technology, Moscow, Russia
e-mail: v.drachev@skoltech.ru

V. P. Drachev
University of North Texas, Denton, TX, USA

A. E. Aliev
A. G. MacDiarmid NanoTech Institute, University of Texas at Dallas, Richardson, TX, USA

E. Kamenetskii (ed.), *Chirality, Magnetism and Magnetoelectricity*,
Topics in Applied Physics 138,
https://doi.org/10.1007/978-3-030-62844-4_3

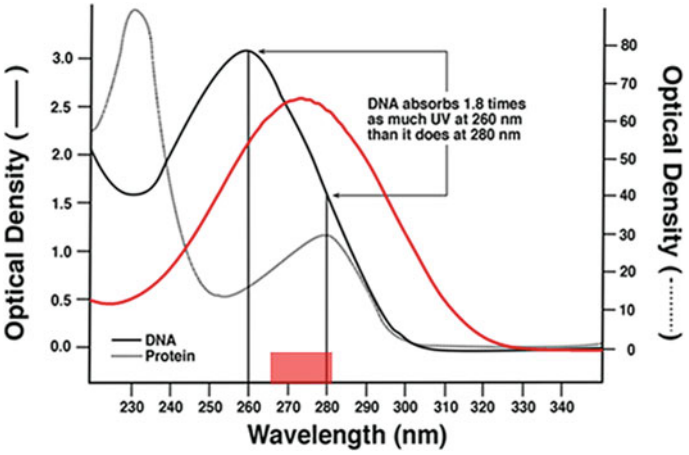

Fig. 3.1 Absorption spectra of DNA (black) and aromatic proteins (gray) (from [3] © Institute of Physics and Engineering in Medicine. Reproduced by permission of IOP Publishing. All rights reserved). The CoNP plasmon resonance in absorption is shown in red, optical density in arbitrary units (from [2] with permission licensed under CC BY 4.0 https://creativecommons.org). The red bar shows the Raman shift range at the laser excitation wavelength 266 nm. The enhancement of the CoNPs will cover this range

in Fig. 3.1, black and gray lines correspondingly) [4–7]. In the resonant Raman condition, where the electronic transition energy of a molecule corresponds to photon energy of Raman excitation light, the Raman scattering intensity of the molecule is enhanced by as much as 10^6 compared to the non-resonant Raman scattering [5]. Because other biological compounds in cells, such as lipids and sugars, are not in the resonant condition at the DUV, Raman scattering from nucleotide bases and aromatic amino acids [4–7] are selectively enhanced in the DUV resonant Raman spectroscopy of cells. Main obstacle of the current resonance Raman approach is that the UV light overdose is harmful to the cells viability and biomolecules functionality [5]. Surface-enhanced resonance Raman scattering (SERRS) will strongly reduce the required energy density for robust detection. Unique combination of plasmonic and magnetic properties makes this platform appropriate for a combined approach of diagnostics and therapy (theranostics). Magnetic nanoparticles represent an attractive tool for medical applications based on their ability to be simultaneously functionalized and guided by an external magnetic field [8–17]. Various biomedical applications of magnetic nanoparticles include enhancing and targeting gene delivery by magnetic force in vitro and in vivo [8, 9], magnetic fluid hyperthermia and cancer therapy [9, 10], cells separation [12], magnetic resonance imaging [13–15]. Biocompatibility of magnetic nanoparticles is under extensive studies and can be achieved by an appropriate coating [16, 17].

Currently plasmonic applications in bio-sensing involve noble metals, Ag or Au, since the quality of their plasmon resonance is highest [18–20]. The SERS protocols based on Ag and Au nanoparticles are demonstrated for tag free protein-protein

binding detection, the feasibility of using SERS to distinguish protein conformational states, which was shown for human insulin and its analog insulin lispro [21–24]. A protocol has been developed to detect cell surface markers, CD44 and CD24, in three breast cancer cell lines [25]. The dielectric functions Ag and Au for this type of nanostructures were carefully studied as well [26–28].

However, Co nanoparticles (Co-NPs), under certain conditions can support an excellent plasmon resonance at about 280 nm with a quality factor greater than Al, In, and comparable to Au in the visible [2]. Importantly, this Co platform is comprising both magnetic and plasmonic properties. A long lasting search for plasmonic materials in the ultraviolet spectral range does not consider Co as a promising candidate [29–32]. One of the criteria for a high quality plasmonic material is that the number of electrons involved in interband transitions must be low, and at the highest possible frequency. These criteria significantly reduces the number of materials that are likely to have favorable optical properties, by the simple fact that all materials with partially occupied d or f states are going to perform poorly across the visible due to interband transitions [33]. Recent works pushed the plasmonics to high-energy range using Al [33–35] and In [36].

The Mott model [37, 38] of conductivity in magnetic metals helps to qualitatively explain observed phenomena for Co nanoparticles. Indeed, the electrical conductivity in metals can be described in terms of two largely independent conducting channels, corresponding to the spin-up and spin-down electrons. Importantly, the probability of spin-flip scattering processes in metals is normally small as compared to the probability of the scattering processes in which the spin is conserved. This means that the spin-up and spin-down electrons do not mix over long distances and, therefore, the electrical conduction occurs in parallel for the two spin channels. *Also*, the scattering rates in ferromagnetic metals of the spin-up and spin-down electrons are quite different, whatever the nature of the scattering centers is. These two channels of conductivity with a distinct spin-dependent scattering is the primary origin of giant magnetoresistance [39].

Here, we discuss the effect of spin polarization on plasmon oscillations of the free electrons in nanoparticles, which is, crucial in many envisioned applications at the cross road of magnetism and plasmonics.

3.2 Spin Polarization in Co Nanoparticles

A new type of plasmons is specific for spin-polarized magnetic nanoparticles. One can expect two independent plasmons which co-exist in a spin-polarized metal nanoparticle following Mott's model. These two plasmons coexist in a particle at the same frequency and polarizations of excitation, but for electrons of opposite spin. Internanoparticle interactions completely demolish plasmon quality resonance, which is the probable reason why it was not observed previously and why the results for bulk films [1] cannot be used for single domain nanoparticles evaluations. It is known

that the exchange interaction of electrons splits the energy bands between spin-up (majority) electrons and spin-down (minority) electrons. We suggest that a low quality of the plasmon resonance for spin-down electrons is due to the large relaxation rate of the conduction electrons caused by high density of empty states in a partially populated d-band. However, the majority electrons with a completely filled d-band does not affect the relaxation rate and plasmon resonance of the conduction spin-up electrons within magnetic nanoparticles.

Figure 3.2 shows spin polarization for bulk Co and Co nanocluster calculated using density functional theory (DFT) simulations. Transition metals are challenging for DFT, since standard exchange-correlation (XC) functional approximations, local density approximation (LDA) and generalized gradient approximation (GGA) underestimate localization of valence d-electrons. This problem is commonly addressed via ad hoc inclusion of a Hubbard correction to e.g. GGA with an effective U term (GGA+U). The resulting GGA+U method has the same low computational cost as GGA. U is a parameter that can be tuned to reproduce experimental results, in particular lattice parameters and magnetic moments. Although optimal U have been suggested in the literature for various metals including Co, [40, 41] not all properties can be reproduced with good accuracy at the same time. Moreover, the value of the U parameter depends on the coordination of metal atoms. Therefore, a different value of U may be required to describe metal bulk and clusters.

In Fig. 3.2 projected density of states (DOS) for the bulk hexagonal close packed (hcp) cobalt (panel b) and a 48-atom cluster (panel a) are shown. DOS for face-centered cubic (fcc) crystal structure looks qualitatively similar. For this comparison we used DFT with the Perdew–Burke-Ernzerhof (PBE) exchange-correlation functional [42]. All calculations are done with all-electron full-potential electronic-structure package FHI-aims [43–46] with "tight" numerical settings. The hcp lattice constants were optimized with PBE. The initial atomic structure of the cluster is obtained using Wulff construction for hcp Co, [47, 48] and then fully relaxed. Projected DOS for the cluster is calculated using Gaussian width of 0.01 eV.

As can be seen in Fig. 3.2, the general shapes of DOS for bulk and particle for both spin channels are similar, but there are also important differences. In particular,

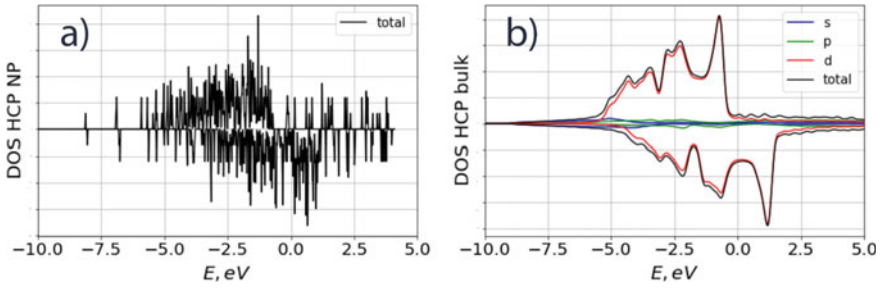

Fig. 3.2 Projected density of states (DOS) for **a** 48-atom Co cluster and **b** bulk hexagonal close packed (hcp) cobalt. Projections on valence s, p, and d orbitals of Co are shown. Spin-minority DOS is shown with negative sign. Zero on the energy axis corresponds to the Fermi level

more structure is observed for the particle both below and above the Fermi level (corresponding to 0 eV). This is not surprising, since the particle has additional states due to the presence of the surface. Notably, the pronounced peaks around the Fermi level in both spin channels are discrete and broadened in the cluster compared to bulk.

3.3 Methods

In this work, the oleic acid (OA) coated cobalt nanoparticles were fabricated by the high temperature reduction of cobalt salt in the presence of trioctylphosphine (TOP) as a surfactant and lithium triethylborohydride as a reducing reagent [49–51]. Cobalt nanoparticles were synthesized using a method similar to that of Sun and Murray [52]. The reduction of cobalt nanoparticles was conducted under inert atmosphere. At room temperature, 0.13 g (0.019 M) of anhydrous cobalt chloride, 0.3 mL (0.018 M) of oleic acid and 30 mL (1.87 M) of dioctyl ether were mixed together under purged nitrogen gas in the three-necked flask containing magnetic stir bar and heated to 100 °C. Then 1.5 mL (0.063 M) of trioctylphosphine, which was injected via syringe and the temperature raised to 205 °C. At this temperature, a strong reducing reagent, 1.5 mL (0.236 M) lithium triethylborohydride, was added in solution and the cobalt nanoparticles begin to grow immediately. The blue colour of the solution turns to black upon nucleation and growth of cobalt nanoparticles. The reaction was terminated by cooling the solution to room temperature and 20 mL (4.8 M) of anhydrous ethanol was added to precipitate the particles. The solution was aged overnight at room temperature in order to attach cobalt nanoparticles to the magnetic stir bar in the flask. The cobalt nanoparticles are removed from a magnetic stir bar and washed several times with ethanol by centrifugation. Finally, oleic acid coated cobalt nanoparticles were suspended in 8 mL of hexane.

To address the mechanism of new type of plasmons specific for magnetic nanoparticles our work involves the structural electron microscopy, superconducting quantum interference device (SQUID) magnetometry, dynamic light scattering (DLS), and spectroscopy of Co nanoparticles. The structural and magnetic characterizations prove the single-domain and superparamagnetic properties of nanoparticles required for spin dependent channels of plasmon oscillations. The magnetic field induced aggregation of nanoparticles in our experiments results in the suppression of the resonance quality.

3.4 Structural Properties

The scanning electron microscopy (SEM) energy dispersive X-ray (EDX) *image* of the cobalt nanoparticles synthesized by the high temperature decomposition of cobalt salt (Fig. 3.3).

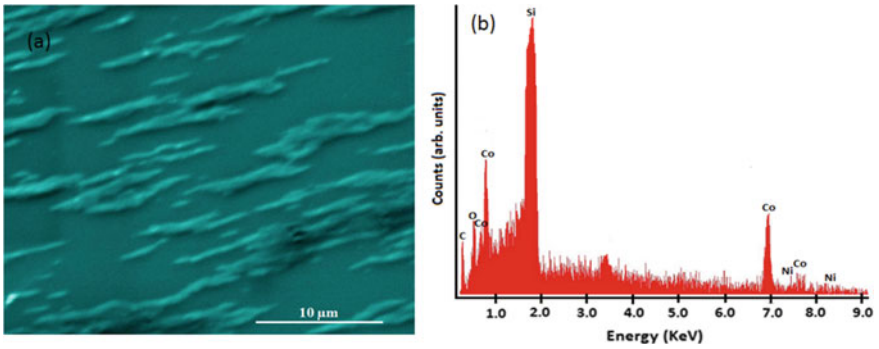

Fig. 3.3 **a** SEM image of the Co nanoparticles. **b** Corresponding EDX spectrum. From [2] with permission licensed under CC BY 4.0 https://creativecommons.org

We observed the large aggregates of cobalt nanoparticles instead of isolated particles because the circular magnet placed underneath the silicon substrate attracted the magnetic nanoparticles from the solution. An energy dispersive X-ray (EDX) spectrum analysis has been obtained from the cobalt nanoparticle sample. This spectrum clearly shows the presence of cobalt peaks. In addition, EDX spectrum also shows the presence of nickel peaks because the sample was made conducting by coating with nickel.

High resolution transmission electron microscopy (TEM) images were obtained with the FEI Tecnai G2 F20 S-Twin 200 keV field emission scanning transmission electron microscope (S/TEM). The high magnification TEM image of spherical cobalt nanoparticles shows the size distribution of cobalt nanoparticles ranges from 6 to 12 nm with average particle diameter of 8.7 nm. High resolution TEM images show that our particles form both hcp and fcc crystal structure. Figure 3.4a shows

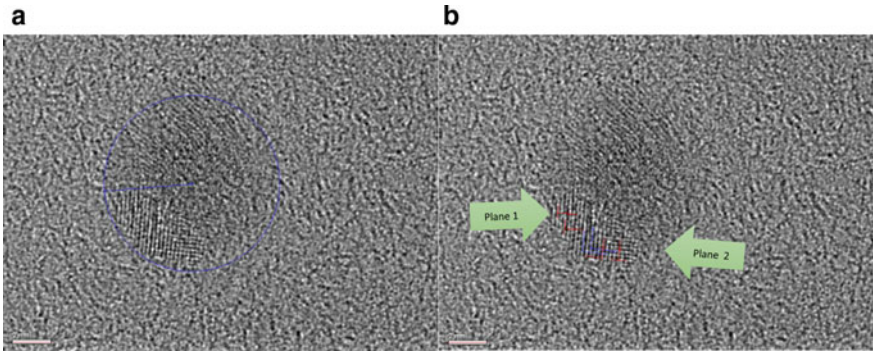

Fig. 3.4 **a** High resolution TEM pattern of [100] hcp crystal structure of Co nanoparticle. The radius here measures 4.59 ±0.05 nm. **b** High resolution TEM pattern of [100]—[001] hcp crystal structure of Co nanoparticle. Plane 1: 0.216 nm ±0.05 nm, Plane 2: 0.223 nm ±0.05 nm, interplanar angle 91.8° ±3°. Calculated: [100] 0.217113, [001] 0.217113, [100]—[001] angle 90°

TEM of [100] crystal structure of some cobalt nanoparticles have lattice spacing 2.102 Å and inter-planar angle 83.6° typical for hcp. Figure 3.4b shows high resolution TEM image of [111] crystal structure of other cobalt nanoparticles has lattice spacing 1.95 Å and inter-planar angle 25.63°, typical for fcc.

For calculation expressions explaining the basic crystallography of cobalt was used [53]. Following by definition, if two planes have indices (hkl) the distance perpendicularly between them is shown by the inverse of the magnitude of the lattice vector.

$$d_{hkl} = \frac{1}{\left|h\boldsymbol{a}^* + k\boldsymbol{b}^* + l\boldsymbol{c}^*\right|} \tag{3.1}$$

Then:

$$\left|h\boldsymbol{a}^* + k\boldsymbol{b}^* + l\boldsymbol{c}^*\right|^2 = \left(h\boldsymbol{a}^* + k\boldsymbol{b}^* + l\boldsymbol{c}^*\right) \cdot \left(h\boldsymbol{a}^* + k\boldsymbol{b}^* + l\boldsymbol{c}^*\right)$$

$$= h^2\boldsymbol{a}^{*2} + k^2\boldsymbol{b}^{*2} + l^2\boldsymbol{c}^{*2} + 2kl\boldsymbol{b}^* \cdot \boldsymbol{c}^* + 2lh\boldsymbol{c}^* \cdot \boldsymbol{a}^* + 2hk\boldsymbol{a}^* \cdot \boldsymbol{b}^*$$

$$= h^2a^{*2} + k^2b^{*2} + l^2c^{*2} + 2klb^*c^* \cos\alpha^* + 2lhc^*a^* \cos\beta^* + 2hka^*b^* \cos\gamma^*$$

here, $\boldsymbol{a}^*$,$\boldsymbol{b}^*$, and $\boldsymbol{c}^*$ are lattice vectors, α^* is the angle between lattice vectors $\boldsymbol{b}^*$ and $\boldsymbol{c}^*$, β^* is the angle between $\boldsymbol{c}^*$ and $\boldsymbol{a}^*$. Knowing that cobalt is found primarily in two phases, hexagonal close packed and face-centered cubic further expansion of this formula was used only for those two overall structures. The lattice constants used for cobalt are found in a variety of literatures. For hcp lattice constants of $a = b = 0.2507$ nm, $c = 0.4069$ nm. For fcc lattice constants of $a = b = c = 0.35446$ nm. First calculations were done to families of standard planes for both fcc and hcp structures. Hexagonal first:

$$\alpha^* = \beta^* = 90°,\ \gamma^* = 60° \text{ and } a^* = b^*, d_{hkl}^2 = \frac{1}{(h^2 + k^2 + hk)a^{*2} + l^2c^{*2}} \tag{3.2}$$

$$\cos\phi = d_{hkl}d_{h'k'l'}\left[\left\{hh' + kk' + \frac{1}{2}(hk' + kh')\right\}a^{*2} + ll'c^{*2}\right]$$

In which:

$$a^* = \frac{2}{a\sqrt{3}}, c^* = \frac{1}{c}$$

Next for cubic:

$$\alpha^* = \beta^* = \gamma^* = 90° \text{ and } a^* = b^* = c^*, d_{hkl}^2 = \frac{1}{(h^2 + k^2 + l^2)a^{*2}} \tag{3.3}$$

$$\cos\phi = \frac{hh' + kk' + ll'}{\sqrt{h^2 + k^2 + l^2}\sqrt{h'^2 + k'^2 + l'^2}} \tag{3.4}$$

In which:

$$a^* = \frac{1}{a}$$

Using these equations [53] the calculated interplanar distances and then angles were able to be deduced. These equations were used to code a simple Mathematica program that would output both interplanar distances as well as angles.

The analysis of the TEM images showed and confirmed the likely structure of cobalt. Though, a large amount of the images had planes and angles that were inconclusive the data definitely points most directly at hexagonal close packed to be the average crystalline phase of the particles. The large amount of inconclusive interplanar angles are likely due to surface deformities, as well as, small and unpredictable tilts in the particles. This would allow for the interplanar angles and distances to be skew, reduced in the case of the interplanar distances and increased up to 180° in the case of the interplanar angles. In general, cobalt should not be found in face-centered cubic crystalline phase below 400 °C. However, some nanoparticles in our case did show possible indications of being in this phase.

3.5 Magnetic Response

Magnetic properties of Co-NP embedded into poly(methyl methacrylate) (PMMA) host matrix were measured using direct current (DC) option of 7 Tesla SQUID magnetometer (Magnetic Property Measurement Device, Quantum Design Inc.). Figure 3.5 shows the step-by-step sample preparation for magnetic measurements: Co-NP collected from magnetic stirring bar were dispersed in PMMA, deposited on a substrate, dried, and then the PMMA film with embedded Co-NP were packed into a gelatine capsule. To reduce the influence of the sample shape (demagnetization effect), all Co-NP embedded sheets were placed in gelatine capsule parallel to the applied magnetic field.

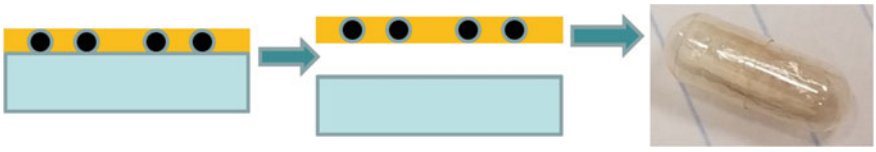

Fig. 3.5 Sample fabrication steps for magnetic measurements. From [2] with permission licensed under CC BY 4.0 https://creativecommons.org

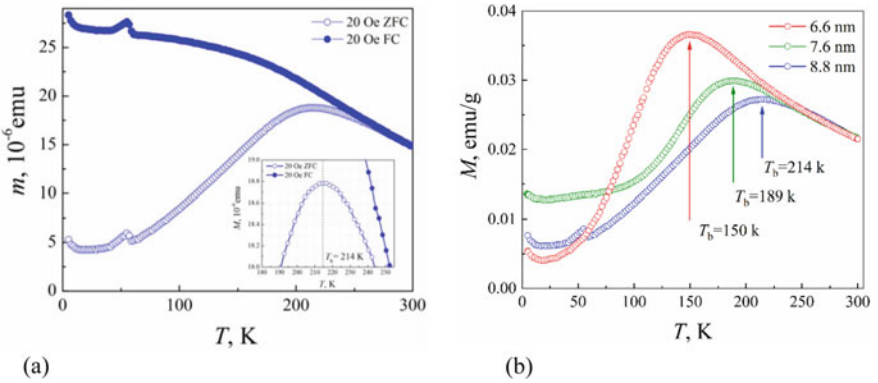

Fig. 3.6 **a** Temperature dependence of magnetic moment for 8.8 nm Co-NP measured in FC (solid blue circles) and ZFC (open blue circles) regimes at applied field of 20 Oe (sample #25). The inset shows an expanded view at a peak of ZFC magnetization. The small bump at 52 K indicates an oxygen contents in the sealed capsule. **b** Shift of ZFC magnetization peaks towards lower temperatures for decreasing particle sizes: 8.8 nm for sample #25; 7.6 nm for sample #28; and 6.6 nm for sample #33, respectively. From [2] with permission licensed under CC BY 4.0 https://creativecommons.org

The temperature dependence of magnetization in field cooling (FC) and zero field cooling (ZFC) regimes exploited to determine the blocking temperature (T_b) at which the ZFC magnetization shows a pronounced peak. T_b is the temperature below which the magnetization curve shows the hysteresis and above superparamagnetic properties [54]. The observed curves for FC and ZFC regimes shown in Fig. 3.6a, b are typical for single-domain ferromagnetic nanoparticles.

For very small particles at finite temperatures the magnetic anisotropy energy, K_u, becomes comparable to the thermal energy resulting in random flip of the magnetization direction and in superparamagnetic (SP) relaxation. Thus, the T_b is defined as the temperature at which the SP relaxation time (response of magnetic dipole), equals the timescale of the experimental technique used to study the magnetic properties, $\omega\tau = 1$. The SP relaxation time τ, also called the Neel relaxation time, τ_N [54], given by [55],

$$\tau = \tau_0 \exp\left(\frac{K_u V}{k_b T}\right). \tag{3.5}$$

was measured using ACMS option of Physical Property Measurement Device (Quantum Design Inc.) in the frequency range of $10 \leq f \leq 10^4$ Hz with alternating current (AC) magnetic field amplitude of ± 10 Oe. Here, K_u is the magnetic anisotropy energy, V is the particle volume, k_B is Boltzmann's constant and T is the temperature. The value of τ_0 extracted from the linear extrapolation of τ to zero $1000/T$ for Co-NP with 6.6 nm in diameter is 4.1×10^{-14} s (see Fig. 3.7). Here we ignore the temperature dependence of τ_0, as it is small compared to the effect of the temperature

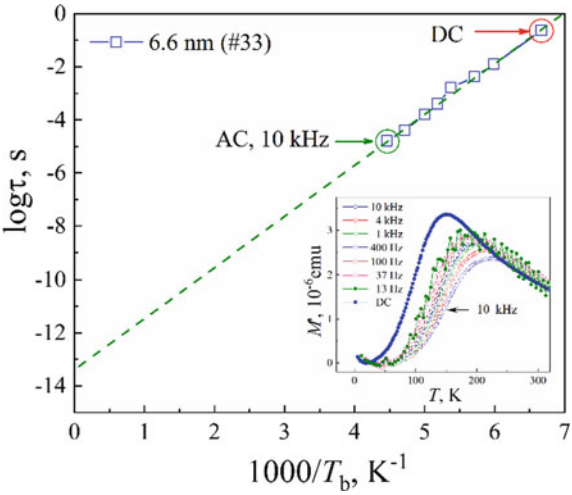

Fig. 3.7 Thermal variation of a relaxation time versus reciprocal temperature for $d = 6.6$ nm (sample #33). The green dashed line is an extrapolation of relaxation time to $1000/T_b = 0$. The inset shows the ZFC magnetization curves measured for each frequency ($f = 1/2\pi\tau$) shown in the main panel. From [2] with permission licensed under CC BY 4.0 https://creativecommons.org

through the exponential [56]. Hence, for DC measurements, where $\ln(\tau/\tau_0) \approx 29$, the blocking temperature, above which the single domain Co-NP starts randomly flip its magnetic moment and is small enough to display superparamagnetism, should roughly satisfy the relationship

$$T_b \approx \frac{K_u V}{29 k_B}. \tag{3.6}$$

With a knowledge of average particle diameter from the precise analysis of TEM images and dynamic light scattering measurements ($d_{\#25} = 8.8$ nm, $d_{\#28} = 7.6$ nm, $d_{\#33} = 6.6$ nm,) the magnetic anisotropy energy extracted from Fig. 3.6b ($K_u^{\#25} = 2.74 \times 10^6$ erg/cm^3, $K_u^{\#28} = 3.73 \times 10^6$ erg/cm^3, $K_u^{\#33} = 3.9 \times 10^6$ erg/cm^3) falls between bulk fcc and hcp structures (2.7×10^6 erg/cm^3 for fcc and 4.7×10^6 erg/cm^3 for hcp), respectively.

The increase in anisotropy constant (energy) for small Co-NP and clusters is resulted from strong contribution of surface atoms. The fraction of Co atoms on the surface of nanoparticles increases with decrease in particle size, which results in decrease of coordination number of surface atoms, increased spin and orbital magnetic moments towards free atoms [57]. The anisotropy energy, K_u, is also increases due to the reduction of spherical symmetry of small nanoparticles [58].

Above the blocking temperature the susceptibility is precisely follows the Curie law, $\chi \sim C/T$, where $C = n(\mu_0\mu)^2/k_B$ is the Curie constant, n is number of particles, μ_0 is magnetic moment of vacuum, and μ is the relative magnetic moment of Co-NP. The linearity of $\chi \sim T_c/T$ plot observed for studied Co-NP (see Fig. 3.8) also implies a low interaction between nanoparticles. The interaction between nanoparticles is a crucial parameter determining the strength of plasmon resonance in Co-NP.

The correctly measured T_b should increase as a cub of the particle diameter, $T_b \sim V \sim D^3$. The deviation of T_b dependence from cubic behaviour in Fig. 3.9a implies

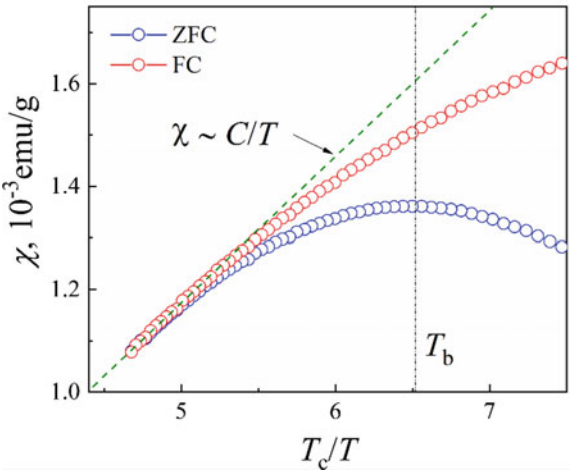

Fig. 3.8 ZFC and FC susceptibility ($\chi = M/H$) for 8.8 nm Co-NP (#25) measured at applied magnetic field of 20 Oe plotted versus reciprocal temperature, $T_c = 1394$ K is the Curie temperature for bulk Co. From [2] with permission licensed under CC BY 4.0 https://creativecommons.org

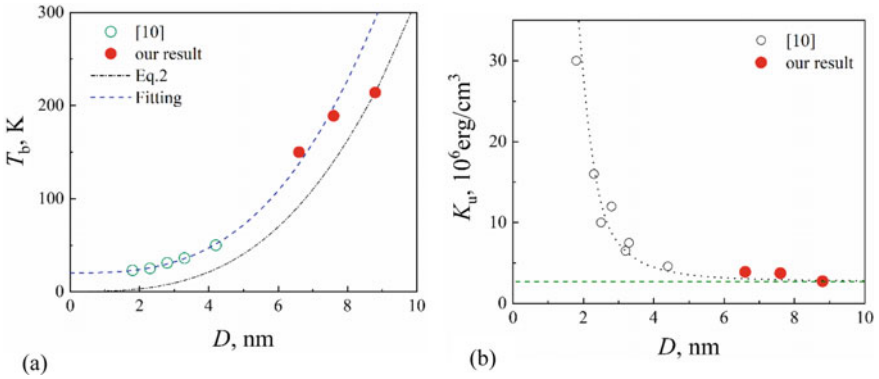

Fig. 3.9 **a** The particle diameter dependence of the blocking temperature, T_b. Dashed and dash-dot curves show a fitting to the cub dependence, $T_b \sim V$. **b** The particle diameter dependence of the anisotropy energy. The dot line is a fitting of reciprocal-cub dependence for [58] and our result. The bulk value for fcc cobalt is shown by dashed (green) line. From [2] with permission licensed under CC BY 4.0 https://creativecommons.org

the decrease of anisotropy energy. On the other hand, the increase of particle size above single-domain size should bring the anisotropy constant towards the balk value [58]. Figure 3.9b shows that for particles larger than 8 nm the anisotropy energy is close to the bulk fcc value, 2.7×10^6 erg/cm^3.

Co nanoparticles coated with CoO (or partially oxidized during fabrication) should exhibit exchange anisotropy due to an interfacial interaction between ferromagnetic

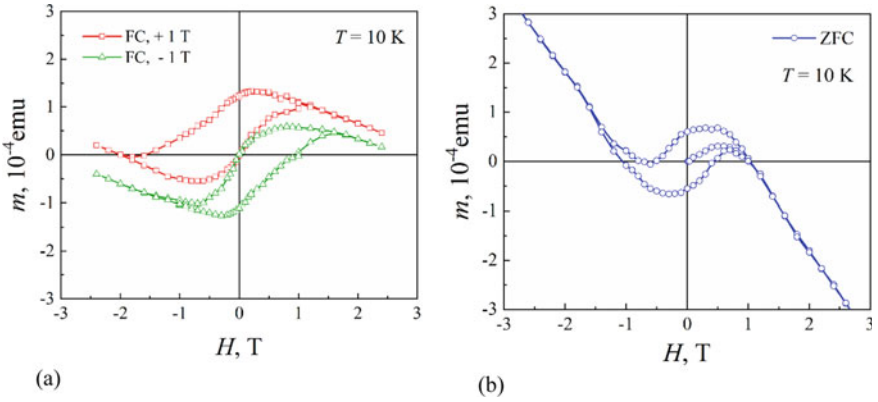

Fig. 3.10 **a** The shift of magnetization loops for sample #25 cooled in field +1 T (open red squares) and −1 T (open green triangles), $T = 10$ K. **b** The magnetization loop for the same sample cooled in zero field is symmetrical. The diamagnetic slope of $m(H)$ curves beyond the hysteresis loop comes from a PMMA matrix. From [2] with permission licensed under CC BY 4.0 https://creativecommons.org

Co metal and antiferromagnetic CoO. The shift of the symmetry of hysteresis loop measured at low temperatures (10 K), after the sample was cooled in a magnetic field of 1 T (FC), implies that CoO shell was formed on the particle surfaces (see Fig. 3.10a). At the same time, the ZFC cooled sample shows quite symmetrical hysteresis loop at $T = 10$ K (see Fig. 3.10b). These measurements were taken for samples #25 (8.8 nm) four months later from preparation date. Since the samples were embedded into PMMA matrix, the oxidation, perhaps, comes from the surfactant shell on the surface of Co-NP. However, as prepared samples measured within 2–3 weeks do not show any shift of the hysteresis loop.

The high-field magnetic moment for 8.8 nm Co-NP (#25) measured at 5, 100 and 298 K are shown in Fig. 3.11a. The analysis of saturation magnetization (M_s) at 5 K (the diamagnetic contribution of PMMA matrix was subtracted) shows that the Co-NP exhibit no-saturation behaviour up to highest available field of 7 T. The saturation magnetization obtained from the extrapolation of M versus $1/H$ line to 0 gives ~10 emu/g, which is close to the value obtained for 7.8 nm Co-NP having fcc structure produced by the Kraschmer carbon arc process [59]. At the same time, this value is one order lower than for bulk fcc Co (162 emu/g, or 175 emu/g, see in [60]). The reduced remanence, $M_r/M_s = 0.02$, is far below of theoretical values for nanocrystals having uniaxial anisotropy such as cobalt in the hcp form (0.5) or in the fcc form (0.8) [60].

Among the possible explanations for the reduced saturation magnetization and remanence is the multiphase (fcc–hcp) crystalline domain structure of single particle separated by amorphous cobalt and the exchange coupling between adjacent Co-NP. The dipole coupling enhancements are attributed to the long-range order of the 2D lattice (particles are embedded into thin PMMA film) and collective “flips” of the

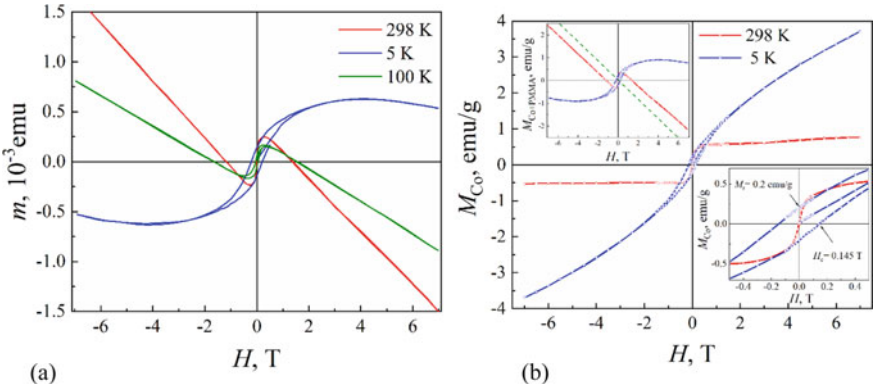

Fig. 3.11 **a** The field dependence of magnetic moment of Co nanoparticles (0.69 mg) dispersed in 10.31 g PMMA matrix taken at 5 K (blue line), 100 K (green line) and 298 K (red line). **b** The field dependence of magnetization for 5 K and 298 K. Main panel shows magnetization of Co-nanoparticles with subtracted diamagnetic contribution of PMMA host material. Top-left inset shows as-measured magnetization at 5 and 298 K. Green dashed line shows the reference line for diamagnetic contribution of host material. Bottom-right inset shows expanded view of magnetization at low fields. From [2] with permission licensed under CC BY 4.0 https://creativecommons.org

magnetic dipoles. On the other hand, the coercive field at $T = 5$ K, $H_c = 0.145$ T, is comparable to reported fcc CoNP [60].

The magnetic moment per particle was calculated for 8.8 nm Co-NP (#25) from the susceptibility χ above the blocking temperature at low field using following equation [58]

$$\chi = \frac{M_s \mu}{3k_b T}, \tag{3.8}$$

where μ is the magnetic moment per particle, M_s is the saturation magnetization, and k_b is Boltzmann's constant. The diamagnetic susceptibility of the PMMA matrix was measured and subtracted to obtain these results: At 214 K contribution of diamagnetic part (PMMA) for sample #25 is 0.45×10^{-6} emu; Magnetic moment, $m = (18.8-0.45) \times 10^{-6}$ emu $= 18.35 \times 10^{-6}$ emu; Saturation magnetization M_s at $T =$ 298 K (the same at 214 K): $M_s = 0.57$ emu/g. Susceptibility χ measured for applied field $H = 20$ Oe at 214 K: $\chi = m/(m_\rho \cdot H) = 18.35 \times 10^{-6}/(0.69 \times 10^{-3} \times 20$ Oe) $= 1.33 \times 10^{-3}$ emu/g Oe. Here $m_\rho = 0.69$ mg is the mass of Co nanoparticles in PMMA host material (10.31 mg). Thus, the magnetic moment per particle above $T = 214$ K:

$$\mu = \frac{3k_B T \chi}{M_s} = \frac{3 \cdot 1.38 \cdot 10^{-16} \cdot 214 \cdot 1.33 \cdot 10^{-3}}{0.57} \cong 2.07 \cdot 10^{-16} \text{ Erg/G} \tag{3.9}$$

Number of Bohr magnetons: $n = \mu/\mu_b = 2.07 \times 10^{-16}/9.27 \times 10^{-21} = 22300$, which is ~$0.687\mu_b$ per atom. Number of Co atoms in single particle, n_a, was calculated as follows: $m_{(Co\ atom)}$ = mol. weight/N_A = 58.933 g/mol/6.022×10^{-23} atom/mol = 9.786×10^{-23} g/atom. Thus, $n_a = m_{particle}/m_{(Co\ atom)} = 3.175 \times 10^{-18}/9.786 \times 10^{-23} = 32444$.

The above number of Bohr magnetons per atom in single 8.8 nm nanoparticle is much lower than the number of Bohr magnetons per single atom in bulk cobalt (300 K), $1.67\mu_b$ (fcc) and $1.73\mu_b$ (hcp). Partially it is caused by demagnetization factor, $N_d = 1/3$, for spherical, non-interacting particles. Note, the demagnetization does not affect the M_s in (3.8), but only χ measured at low fields, $\chi = \chi_{eff}(1+N_d)$. Thus, taking into account the demagnetization factor results in $0.96\mu_b$ per atom.

3.6 Optical Resonance in Spin-Polarized Co Nanoparticles

Good quality plasmon resonance in absorption is proven below to be the property of isolated Co nanoparticles. Indeed, we observe a complete suppression of sharp plasmon resonance for aggregated Co nanoparticles, probably due to the interparticle interaction inducing a spin-flip electron scattering at the particle surface. This behavior is reversible, i.e., the sharp resonance is totally restored for separated nanoparticles after sonication, as shown below. Note, that the absence of cobalt oxide shell, which could introduce an antiferromagnetic response, is controlled with the low temperature SQUID measurements.

The ab-initio simulations of the relaxation constants performed for the giant magnetoresistance show big difference for spin-up and spin-down electrons [61, 62]. Susceptibility of Co nanoparticles can be expressed as a sum of two terms coming from two independent group of electrons, thus the total polarizability is given by:

$$\alpha = r^3(\chi_\uparrow + \chi_\downarrow) = r^3\left(\frac{1}{X_\uparrow + i\delta_\uparrow} + \frac{1}{X_\downarrow + i\delta_\downarrow}\right) \tag{3.10}$$

Here we use the spectral representation of the Drude-Sommerfield model [63, 64].

$$\chi_i = \frac{\varepsilon_h - \varepsilon_{mi}}{2\varepsilon_h + \varepsilon_{mi}} = \frac{1}{X_i + i\delta_i},\ \varepsilon_{mi} = \varepsilon_{0i} - \frac{\omega_p^2}{\omega(\omega + i2\Gamma)},\ \varepsilon_h \approx \varepsilon_0,\ \omega_{sp}^2 = \frac{\omega_p^2}{\varepsilon_0 + 2\varepsilon_h} \tag{3.11}$$

$X_i = \frac{\omega_{sp}^2 - \omega^2}{\omega_{sp}^2}$, $\delta_i = \frac{\omega 2\Gamma_i}{\omega_{sp}^2}$, $2\Gamma_\uparrow = \upsilon_F/\lambda_\uparrow$ and $2\Gamma_\downarrow = \upsilon_F/\lambda_\downarrow$, where $\lambda_\uparrow$ = 12 nm, $\lambda_\downarrow$ = 0.6 nm, Fermi velocity $\upsilon_F = 2.1 \times 10^5$ m/s, thus $2\Gamma_\uparrow \approx 72.4$ meV and $2\Gamma_\downarrow \approx 1448$ meV [61, 62]. Extinction cross-section is kImα. Thus, the absorption spectra should look like a sharp resonance, due to spin-up electrons, plus a

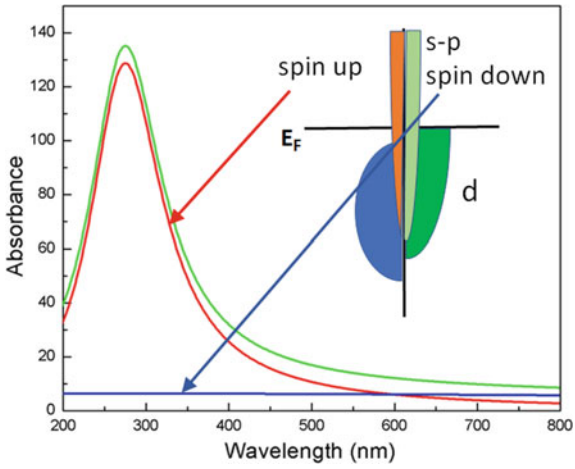

Fig. 3.12 Two plasmon model for Co nanoparticles absorbance. ω_{sp} is taken 280 nm. Green is the sum of red (spin up) and blue (spin down). Insert: a cartoon of the projected density of states typical for Co. From [2] with permission licensed under CC BY 4.0 https://creativecommons.org

broad background coming from spin-down electrons (Fig. 3.12). Thus, as soon as all possible electron scattering processes go without spin-flip, meaning that two group of electrons are independent, one should expect sharp plasmon resonance. In particular, it requires single domain nanoparticles, since inter-domain walls increase probability of spin flip electron scattering and thus two group of electrons are not independent anymore.

3.7 Effect of Dimers

Experiments show sharp plasmon resonance for isolated, single-domain Co nanoparticles (Co NPs). However, the plasmon resonance disappears, if small, two-three particles aggregates were formed. The magnetization measurements by SQUID system show superparamagnetic properties of the Co NPs at room temperature, which indicates the single-domain structure. The temperature dependence of the magnetization gives blocking temperature, which corresponds to the particle volume of this size. Below the blocking temperature field dependence of the magnetization has hysteresis behavior. The shift of the hysteresis loop cooled to 10 K at field $+1$ T and opposite shift for the sample cooled at -1 T allows to control the oxidation level of nanoparticles. All the results below correspond to the particles without oxide shell. Figure 13a demonstrates remarkable resonance quality of the representative spectrum for Co NPs in hexane solution shown in red. The plasmon resonance quality is about the same as for gold nanoparticles, which have resonance in the green spectral range. Co-NPs are isolated due to surfactants, trioctylphosphine and oleic acid. Dynamic light scattering data show an average size close to the mean size from TEM images.

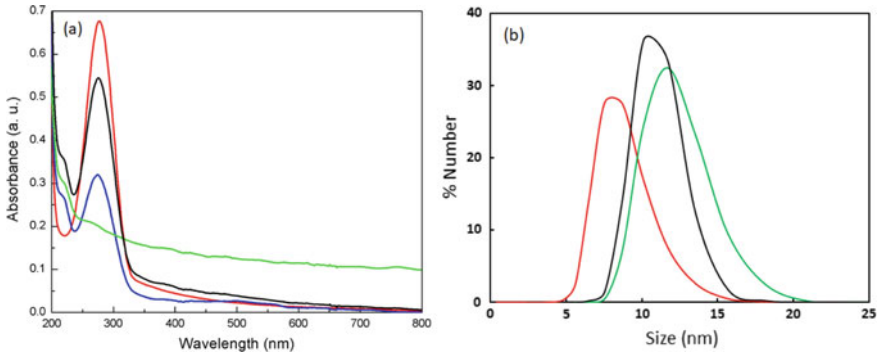

Fig. 3.13 **a** Experimental absorbance of Co-NPs in hexane. As grown Co-NPs (red), after 1 h sonication with external 130 mT DC magnetic field (blue), after 2.5 h sonication with external 130 mT DC magnetic field (green, plasmon peak is demolished), magnetic field is off and 1 h sonication (black). **b** Co-NPs size distribution measured with dynamic light scattering (red)-as grown; (green) -2.5 h sonication with external 130 mT DC magnetic field; (black) after 1 h sonication without magnetic field. From [2] with permission licensed under CC BY 4.0 https://creativecommons.org

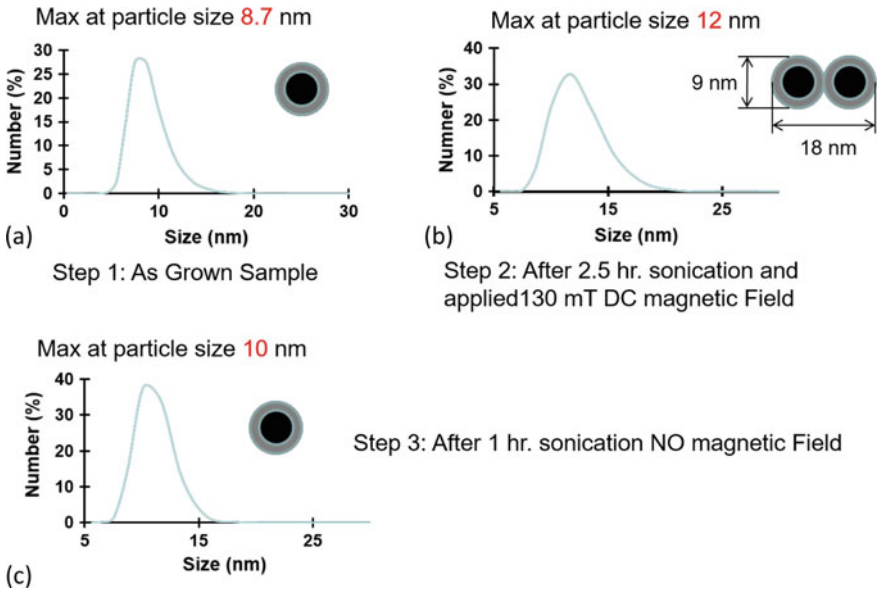

Fig. 3.14 Dynamic light scattering (DLS) size distribution of Co nanoparticles (**a**), as grown sample; (**b**), after 2.5 h sonication with external 130 mT DC magnetic field; and (**c**), after 1 h sonication without external magnetic field. From [2] with permission licensed under CC BY 4.0 https://creativecommons.org

Shown in Fig. 3.14 are dynamic light scattering (DLS) results on particle size distribution of undiluted Co nanoparticles samples. As grown Co nanoparticles have DLS average particle size 8.7 nm. Then, the solution was sonicated in the presence of 130 mT external DC magnetic field. The effective particles size has been increased from 8.7 nm to 12 nm. This increase in particle size is due to agglomeration of Co nanoparticles in the presence of magnetic field. To reverse the agglomeration, the sample was sonicated for 1 h in the absence of an external DC magnetic field. The particle size has been reduced down to 10 nm. When an external field is removed, sonication isolates the nanoparticles and results in decreasing of the effective particle size. The DLS measurements were performed at the same time as collected the optical spectra and prepared sample for magnetometry like in Fig. 3.13.

The following experiment illustrates interaction of Co nanoparticles separated by thin surfactant shell. To initiate aggregation, the 130 mT DC magnetic field together with sonication were applied to the Co NP hexane suspension in a quartz cuvette. After 1 h of "aggregation" the dynamic light scattering and absorption spectra were collected. Figure 3.3 shows reduced plasmon peak (shown in blue). After 2.5 h sonication in magnetic field plasmon peak disappeared (shown in green). The dynamic light scattering shown in the Fig. 3.3b gives increase in the hydrodynamic particles size from 8.7 to 12–13 nm corresponding to small, two-three particles aggregates. Remarkable, that the following up sonication, without external magnetic field, separates aggregated particles and the plasmon resonance is restored. Thus, this magnetic/sonication induced aggregation is a reversible process.

The magnetization of as grown, after aggregation, and after sonication without magnetic field samples, shown in Fig. 3.15, also demonstrate a reversible behavior. It first decreases after 2.5 h of sonication in magnetic field (Fig. 3.15 blue line), then return to the initial value after sonication without magnetic field (Fig. 3.15 black line).

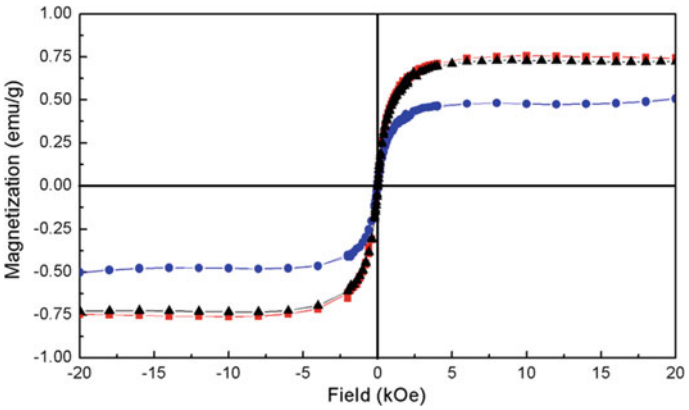

Fig. 3.15 Magnetization of Co-NPs embedded in PMMA. As grown Co-NPs (red), after 2.5 h sonication with external 130 mT DC magnetic field (blue), and 1 h sonication with magnetic field off (black). From [2] with permission licensed under CC BY 4.0 https://creativecommons.org

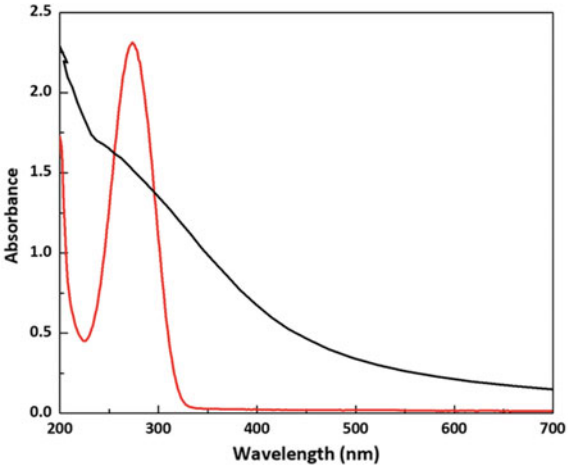

Fig. 3.16 Absorbance of the Co NPs in hexane solution: experiment (red) and calculated (black) using J&C data. [1] From [2] with permission licensed under CC BY 4.0 https://creativecommons.org

Note that calculated absorption spectrum for Co nanoparticles using J&C permittivity for Co films does not show a pronounced resonance (Fig. 3.16 black line) in contrast to the experimental spectrum for single-domain Co nanoparticles (Fig. 3.16 red line). For the nanoparticles with substantially sub-wavelength size the dipole approximation reduces Mie's theory to the following expression for the extinction cross-section [29]:

$$\sigma_{ext} = 9\frac{\omega\varepsilon_h^{1/2}}{c}V\frac{\varepsilon_h\varepsilon_2(\omega)}{[\varepsilon_1(\omega)+2\varepsilon_h]^2+\varepsilon_2^2(\omega)} \tag{3.12}$$

where ω is the light frequency, V is the volume of the spherical particle, ε_h is the dielectric permittivity of the surrounding (host) medium, and c is the speed of light. The spectrum of nanoparticles was calculated using bulk material complex permittivity $\varepsilon(\omega) = \varepsilon_1 + i\varepsilon_2$ from J&C [1]. Note that, this approach for modeling nanoparticles spectra works for nonmagnetic metals like Au, Ag , but cannot be used for Co. One can see that the calculated spectrum using permittivity measured for Co films has no good resonance. That is the reason why Co was not consider as a promising candidate so far. Indeed, if the film has multi-domain structure, where neighbour domains are typically disoriented, the electron scattering easily changes the spin polarization. Thus, electrons with spin-up become with spin-down and immediately got huge increase in relaxation rate due to available empty states in the d-band.

3.8 Conclusions

Spin-polarized metals have two channels of conductivity resulted in interesting applications including the most known giant magnetoresistance. Magnetic nanoparticles have unusual features compared to bulk materials. They manifest superparamagnetic properties in case of single-domain size. They have discrete density of states due to quantum size effect. Our experiments with Co nanoparticles clearly show a new type of plasmon excitation. This type of plasmon has unusual properties due to existence of two independent groups of electrons with opposite spins providing weak interaction so that all electron scattering processes occur without spin flip. Magnetic response of the nanoparticles enables controlled and reversible aggregation accompanied by the tailoring of optical absorption. Magnetic nature of the nanoparticles suggests a new type of these plasmons. Magnetic response of Co nanoparticles shows less magnetic moments per atom relative to the bulk value, namely 0.68 μ_b and taking into account the demagnetization factor 0.96 μ_b per atom versus 1.7 μ_b. The exchange interaction of electrons splits the energy bands between spin-up electrons and spin-down electrons. It makes possible to coexist two independent channels of conductivity as well as two independent plasmons in the same nanoparticle with very different electron relaxation. Indeed, the density of empty states in a partially populated d-band is high, resulting in a large relaxation rate of the spin-down conduction electrons and consequently in low quality of the plasmon resonance. In contrast, the majority electrons with a completely filled d-band do not provide final states for the scattering processes of the conduction spin-up electrons, therefore supporting a good quality plasmon resonance. The scattering without spin flip is required to keep these two plasmons independent.

References

1. P.B. Johnson, R.W. Christy, Optical constants of transition metals: Ti, V, Cr, Mn, Fe Co, Ni, and Pd. Phys. Rev. **9**, 5056 (1974). https://doi.org/10.1103/PhysRevB.9.5056
2. H. Bhata, A.E. Aliev, V.P. Drachev, New mechanism of plasmons specific for spin-polarized nanoparticles. Sci. Rep. **9**, 2019 (2019). https://doi.org/10.1038/s41598-019-38657-w
3. A.R. Young, Chromophores in human skin. Phys. Med. Biol. **42**, 789–802 (1997)
4. G.J. Thomas, Raman spectroscopy of protein and nucleic acid assemblies. Annu. Rev. Biophys. Biomol. Struct. **28**, 1–27 (1999)
5. Y. Kumamoto, A. Taguchi, N.I. Smith, S. Kawata, Deep UV resonant Raman spectroscopy for photodamage characterization in cells. Biomed. Optics Express **2**, 927–936 (2011)
6. H. Takeuchi, UV Raman markers for structural analysis of aromatic side chains in proteins. Anal. Sci. **27**, 1077–1086 (2011)
7. L. Ashton, C.E.M. Hogwood, A.S. Tait, J. Kuligowski, C.M. Smales, D.G. Bracewell, A.J. Dicksone, R. Goodacre, UV resonance Raman spectroscopy: a process analytical tool for host cell DNA and RNA dynamics in mammalian cell lines. J. Chem. Technol. Biotechnol. **90**, 237–243 (2015)
8. F. Scherer, M. Anton, U. Schillinge, J. Henke, C. Bergemann, A. Kruger, B. Gansbacher, C. Plank, Magnetofection: enhancing and targeting gene delivery by magnetic force in vitro and in vivo. Gene Ther. **9**, 102–109 (2002)

9. A.S. Lübe, C. Alexiou, C. Bergemann, Clinical applications of magnetic drug targeting. J. Surg. Res. **95**, 200 (2001)
10. N.A. Brusentsov, L.V. Nikitin, T.N. Brusentsova, F.S. Bayburtskiy, L.I. Shumakov, N.Y. Jurchenko, Magnetic fluid hyperthermia of the mouse experimental tumor. J. Magn. Magn. Mater. **252**, 378 (2002)
11. V.I. Shubayev, T.R. Pisanic, S. Jin, Magnetic nanoparticles for theragnostics. Adv. Drug Deliv. Rev. **61**, 467–477 (2009)
12. C. Jiang, J.B. Wechuck, W.F. Goins, D.M. Krisky, D. Wolfe, M.M. Ataai, J.C. Glorioso, Immobilized cobalt affinity chromatography provides a novel, efficient method for herpes simplex virus type 1 gene vector purification. J. Virol. **78**, 8994–9006 (2004)
13. J.H. Lee, Y.M. Huh, Y.W. Jun, J.W. Seo, J.T. Jang, H.T. Song, S. Kim, Cho, H.G. Yoon, J.S. Suh, J. Cheon, Artificially engineered magnetic nanoparticles for ultra-sensitive molecular imaging. Nat. Med. **13**, 95–99 (2007)
14. L.M. Parkes, R. Hodgson, L.T. Lu, L.D. Tung, I. Robinson, D.G. Fernig, N.T.K. Thanl, Cobalt nanaoprticles as a novel magnetic resonance contrast agent-relaxivities at 1.5 and 3 Tesla. Contrast Media Mol. Imag. **3**, 150–156 (2008)
15. N.A. Frey, S. Peng, K. Cheng, S. Sun, Magnetic nanoparticles: synthesis, functionalization, and applications in bioimaging and magnetic energy storage. Chem. Soc. Rev. **38**, 2532–2542 (2009)
16. L.H. Reddy, J.L. Arias, J. Nicolas, P. Couvreur, Magnetic nanoparticles: design and characterization, toxicity and biocompatibility, pharmaceutical and biomedical applications. Chem. Rev. **112**, 5818–5878 (2012)
17. B. Issa, I.M. Obaidat, B.A. Albiss, Y. Haik, Magnetic nanoparticles: surface effects and properties related to biomedicine applications. Int. J. Mol. Sci. **14**, 21266–21305 (2013)
18. S. Lal, S. Link, N.J. Halas, Nano-optics from sensing to waveguiding. Nat. Photon. **1**, 641–648 (2007)
19. K.A. Willets, R.P. Van Duyne, Localized surface plasmon resonance spectroscopy and sensing Annu. Rev. Phys. Chem. **58**, 267–297 (2007)
20. M. Stockman, Nanophotonics: past, present, and glimpse into future. Opt. Express **19**, 22029–22106 (2011)
21. V.P. Drachev, V.M. Shalaev, Biomolecule sensing with adaptive plasmonic nanostructure, a chapter in a "Surface Enhanced Raman Scattering - Physics and Applications", ed. by K. Kneipp, M. Moskovits, and H. Kneipp, Springer Verlag, Topics in applied physics (2006)
22. V.P. Drachev, V. Nashine, M.D. Thoreson, D. Ben-Amotz, V.J. Davisson, V.M. Shalaev, Adaptive silver films for detection of antibody-antigen binding. Langmuir **21**, 8368–8373 (2005)
23. V.P. Drachev, V.C. Nashine, M.D. Thoreson, D. Ben-Amotz, V.J. Davisson, V.M. Shalaev, Surface-enhanced Raman scattering of biomolecules with adaptive nanostructures. J. Raman Spectrosc. **36**, special issue on SERS, 648–656 (2005)
24. V.P. Drachev, M.D. Thoreson, E.N. Khaliullin, V.J. Davisson, V.M. Shalaev, Surface-enhanced raman difference between human insulin and insulin lispro detected with adaptive nanostructures. J. Phys. Chem. **108**, 18046–18052 (2004)
25. K. Lee, V.P. Drachev, J. Irudayaraj, DNA-Gold nanoparticle reversible networks grown on cell surface marker sites: application in diagnostics. ACS Nano **5**(3), 2109–2117 (2011)
26. V.P. Drachev, A.K. Buin, H. Nakotte, V.M. Shalaev, Size dependent $\chi(3)$ for conduction electrons in Ag nanoparticles. Nano Lett. **4**, 1535 (2004)
27. K.P. Chen, V.P. Drachev, J.D. Borneman, A.V. Kildishev, V.M. Shalaev, Drude relaxation rate in grained gold nanoantennas. Nano Lett. **10**, 916–922 (2010)
28. V.P. Drachev, U.K. Chettiar, A.V. Kildishev, W. Cai, H.-K. Yuan, V.M. Shalaev, The Ag dielectric function in plasmonic metamaterials. Opt. Express **16**, 1186–1195 (2008)
29. U. Kreibig, M. Volmer, Optical properties of metal clusters. Springer-Verlag, Berlin (1995), 532p. https://doi.org/10.1007/978-3-662-09109-8
30. J.M. McMahon, G.C. Schatz, S.K. Gray, Plasmonics in the ultraviolet with the poor metals Al, Ga, In, Sn, Tl, Pb, and Bi. Phys. Chem. Chem. Phys. **15**(15), 5415–5423 (2013)

31. M.G. Blaber, C.J. Engel, S.R.C. Vivekchand, S.M. Lubin, T.W. Odom, G.C. Schatz, Eutectic liquid alloys for plasmonics: theory and experiment. Nano Lett. **12**, 4324–4328 (2012)
32. M.G. Blaber, M.D. Arnold, M.J. Ford, A review of the optical properties of alloys and intermetallics for plasmonics J. Phys.: Condens. Matter **22**, 143201–143215 (2010)
33. G. Maidecchi, G. Gonella, R.P. Zaccaria, R. Moroni, L. Anghinolfi, A. Giglia, S. Nannarone, L. Mattera, H.-L. Dai, M. Canepa, F. Bisio, Deep ultraviolet plasmon resonance in aluminum nanoparticle arrays. ACS Nano **7**, 5834 (2013)
34. M.W. Knight, N.S. King, L. Liu, H.O. Everitt, P. Nordlander, N.J. Halas, Aluminum for plasmonics. ACS Nano **8**, 834–840 (2014)
35. T. Ding, D.O. Sigle, L.O. Herrmann, D. Wolverson, J. J. Baumberg, Nanoimprint Lithography of Al Nanovoids for Deep-UV SERS. ACS Appl. Mater. Interf. https://doi.org/10.1021/am505511v
36. Y. Kumamoto, A. Taguchi, M. Honda, K. Watanabe, Y. Saito, S. Kawata, Indium for deep ultraviolet surface-enhanced resonance raman scattering. ACS Photon. **1**, 598–603 (2014)
37. N.F. Mott, The resistance and thermoelectric properties of the transition metals. Proc. Royal Soc. **156**, 368 (1936). https://doi.org/10.1098/rspa.1936.0154
38. N.F. Mott, Electrons in transition metals. Adv. Phys. **13**, 325 (1964). https://doi.org/10.1080/00018736400101041
39. M.N. Baibich, J.M. Broto, A. Fert, N. Van Dau, F. Petroff, P. Etienne, G. Creuzet, A. Friederich, Chazelas, Giant magnetoresistance of (001) Fe/(001) Cr magnetic superlattices. J. Phys. Rev. Lett. **61**, 2472 (1988). https://doi.org/10.1103/PhysRevLett.61.2472
40. V.A. de la Peña O'Shea, I. de P. R. Moreira, A. Roldán, A. Illas, Electronic and magnetic structure of bulk cobalt: The αα, ββ, and εε-phases from density functional theory calculations.J. Chem. Phys. **133**, 024701 (2010)
41. D. Gull, Electron mean free path in elemental metals. J. Appl. Phys. **119**, 085101 (2016)
42. P. Perdew, K. Burke, M. Ernzerhof, Phys. Rev. Lett. **77**, 3865 (1996)
43. V. Blum, R. Gehrke, F. Hanke, P. Havu, V. Havu, X. Ren, K. Reuter, M. Scheffler, Comput. Phys. Commun. **180**, 2175–2196 (2009)
44. V. Havu, V. Blum, P. Havu, M. Scheffler, J. Comput. Phys. **228**, 8367–8379 (2009)
45. A. Marek, V. Blum, R. Johanni, V. Havu, B. Lang, T. Auckenthaler, A. Heinecke, H.-J. Bungartz, H. Lederer, J. Phys. Condens. Matter **26**, 213201 (2014)
46. S. Levchenko, X. Ren, J. Wieferink, R. Johanni, P. Rinke, V. Blum, M. Scheffler, Comput. Phys. Commun. **192**, 60–69 (2015)
47. J.-X. Liu, H.-Y. Su, D.-P. Sun, B.-Y. Zhang, W.-X. Li, J. Am. Chem. Soc. **135**, 16284 (2013)
48. J.M. Rahm, P. Erhart, WulffPack: a python package for Wulff constructions. J. Open Source Softw. 5.45 (2020): 1944
49. V.F. Puntes, K. Krishnan, A.P. Alivisatos, Colloidal nanocrystal shape and size control: the case of cobalt. Science **291**, 2115–2117 (2001)
50. H.T. Yang, C.M. Shen, Y.G. Wang, Y.K. Su, T.Z. Yang, H.J. Gao, Stable cobalt nanoparticles passivated with oleic acid and trioctylphosphine. Nanotechnology **15**, 70–74 (2004)
51. Y.K. Su, C.M. Shen, T.Z. Yang, H.T. Yang, H.J. Gao, H.L. Li, The dependence of Co nanoaprticle sizes on the ratio of surfactants and the influence of different crystal sizes on magnetic properties. Appl. Phys. A **81**, 569–572 (2005)
52. S.H. Sun, C.B. Murray, Synthesis of monodisperse cobalt nanoparticles and their assemble into magnetic superlattices. J. Appl. Phys. **85**, 4325 (1999). https://doi.org/10.1063/1.370357
53. A. Kelly, K. Knowles (2012) *Crystallography and Crystal Defects* 2nd Ed. (Wiley, 2011)
54. L. Néel, Théorie du traînage magnétique des ferromagnétiques en grains fins avec application aux terres 5 cuites. Ann. Géophys. **5**, 99–136 (1949)
55. W.T. Coffey, D.S.F. Crothers, Yu.P. Kalmykov, E.S. Massawe, J.T. Waldron, Exact analytic formula for the correlation time of a single-domain ferromagnetic particle. Phys. Rev. E **49**, 1869 (1994)
56. J.L. Dormann; F. D'Orazio, F. Lucari, E. Tronc, P. Prene, J.P. Jolivet, D. Fiorani, R. Cherkaoui, M. Nogue's, Thermal variation of the relaxation time of the magnetic moment of γ-Fe_2O_3 nanoparticles with interparticle interactions of various strengths. Phys. Rev. B **53**, 14291–14297 (1996)

57. P. Gambardella, M. Rusponi, M. Veronese, S.S. Dhesi, C. Grazioli, A. Dallmeyer, I. Cabria, R. Zeller, P.H. Dederichs, K. Kern, C. Carbone, H. Brune, Giant magnetic anisotropu of single atoms and nanoparticles. Science **300**, 1130–1133 (2003)
58. J.P. Chen, C.M. Sorensen, K.J. Klabund, Enhanced magnetization of nanoscale colloidal cobalt particles. Phys. Rev. B **51**, 11527 (1995)
59. M.E. Mohenry, S.A. Majetich, J.O. Artman, M. DeGraef, S.W. Staley, Superparamagnetism in carbon-coated Co particles produced by the Kratschmer carbon arc process. Phys. Rev. B **49**, 11358 (1994)
60. C. Petit, Z.L. Wang, M.P. Pileni, Seven-nanometer hexagonal close packed cobalt nanocrystals for high-temperature magnetic applications through a novel annealing process. J. Phys. Chem. B **109**, 15309–15316 (2005)
61. E.Y. Tsymbal, D.G. Pettifor, Perspectives of giant magnetoresistance. in *Solid state Physics*, ed. by H. Ehrenreich, F. Spaepen (Eds), (Academic Press, Boston), 56, pp. 113–237 (2001). https://digitalcommons.unl.edu/physicstsymbal/50
62. D.J. Gall, App. Phys. **119**, 085101–085101–085105 (2016). https://doi.org/10.1063/1.4942216
63. D.J. Bergman, D. Stroud, Properties of macroscopically ingomogeneous media, in *Solid State Physics*, ed. by H. Ehrenreich, D. Turnbull (Academic, Boston), 46, pp. 149–270 (1992)
64. V.A. Markel, L.S. Muratov, M.I. Stokman, Optical properties of fractals: theory and numerical simulation. Sov. Phys. JETP **71**(3), 455–464 (1990)